

# Detection of a radio halo in the Virgo cluster<sup>★</sup>

B. Vollmer<sup>1,2</sup>, W. Reich<sup>2</sup>, and R. Wielebinski<sup>2</sup>

<sup>1</sup> CDS, Observatoire astronomique de Strasbourg, UMR 7550, 11, rue de l'université, 67000 Strasbourg, France

<sup>2</sup> Max-Planck-Institut für Radioastronomie, Auf dem Hügel 69, 53121 Bonn, Germany

Received ; accepted

**Abstract.** New Effelsberg 1.4 GHz observations of the central  $10^\circ \times 10^\circ$  of the Virgo cluster are presented. NVSS data are used to subtract point sources from our map. During the data reduction process special care is taken (i) to disentangle emission from the North Polar Spur from emission from the Virgo cluster, (ii) to disentangle emission from the strong M87 sidelobes from emission from the Virgo cluster, and (iii) to correct for non-linear ground emission due to the long scans. We detect a low surface brightness radio halo with a flux density of  $5 \pm 1.5$  Jy centered close to the elliptical galaxy M86. This halo is much weaker than that observed in the Coma cluster. It is reminiscent of a past interaction between the intracluster medium of M86 and a low density gas, belonging most probably to the Virgo cluster.

**Key words.** Galaxies: clusters: individual: Virgo – intergalactic medium – Radio continuum: general

## 1. Introduction

The location of the largest diffuse radio emission sources in the local Universe are galaxy clusters. A very hot (several  $10^7$  K) and tenuous ( $n \sim 10^{-4} \text{ cm}^{-3}$ ) gas pervades the whole cluster. This gas can be directly observed in X-rays (see e.g. Ebeling et al. 1996). The existence of a cluster-wide diffuse radio emission indicates that there are additional, important components of the intracluster medium (ICM): large-scale magnetic fields and relativistic electrons. In general these extended, diffuse radio sources are divided into two subgroups (see e.g. Giovannini & Feretti 2002a): (i) cluster halos have low surface brightness, are centered on the cluster center, and show a regular shape. Their prototype is Coma C (Deiss et al. 1997). They have a steep spectrum and show a negligible degree of polarization. Their typical size is  $\sim 1$  Mpc. (ii) Relic sources also show low surface brightness and steep spectra, but in contrast to radio halos they are elongated structures that are found at the periphery of the cluster. In addition, their degree of polarization is high. A3667 (Röttgering et al. 1997) represents an extreme member of this group.

Diffuse, extended radio sources are rare. Giovannini et al. (1999), using a complete cluster sample, found that 5% of clusters have radio halos and 6% show relic sources. The X-ray luminosity of clusters hosting a diffuse radio source

is significantly higher than that of clusters without such a source (Giovannini & Feretti 2002b). The number of known diffuse radio sources has significantly increased to about 40 in the last years. Typical radio powers of diffuse sources are  $10^{24} - 10^{25} \text{ W Hz}^{-1}$  at 1.4 GHz. The strength of the magnetic fields calculated using equipartition between the relativistic electrons and the magnetic field is  $0.1 - 1 \mu\text{G}$ .

There is strong evidence that diffuse radio sources are related to cluster mergers. Significant substructure in the X-ray emission is detected in clusters hosting a radio halo/relic (Böhringer & Schücker 2002). At present a merger scenario could not be clearly excluded for a cluster showing a radio halo (Giovannini & Feretti 2002a). The formation of halos and relics is tightly linked to the dynamical behaviour of the cluster. Whereas the magnetic fields and relativistic electron populations are built during the cluster formation and subsequent evolution, the energy supply for the maintenance of the diffuse radio sources is due to recent gravitational interactions between the cluster and an infalling galaxy group or cluster.

One of the best studied cluster radio sources is Coma (see e.g. Deiss et al. 1997), which is located at  $\sim 100$  Mpc distance. Its extent on the sky is about  $1^\circ$ . In order to detect a large-scale, diffuse emission in a galaxy cluster with a single-dish telescope, additional high angular resolution observations at the same wavelength must be available to identify point sources, which have to be subtracted. It must also be taken into account that the region of interest should not be too large, because the low surface brightness of diffuse radio sources implies huge amount of observa-

Send offprint requests to: B. Vollmer: bvollmer@astro.u-strasbg.fr

<sup>★</sup> Based on observations with the Effelsberg 100-m telescope operated by the Max-Planck-Institut für Radioastronomie (MPIfR), Bonn, Germany

tion time at high frequencies. In addition, observations of large areas may have problems in the determination of a constant baselevel. Because of these reasons, it is only now that we attempt to detect a diffuse radio source in the Virgo cluster with the Effelsberg 100-m telescope. The Virgo cluster, with a distance of 17 Mpc<sup>1</sup>, is the nearest galaxy cluster on the northern hemisphere. We cover the central  $10^\circ \times 10^\circ$ .

Virgo is a dynamically young cluster, i.e. the galaxy distribution is not symmetric (see e.g. Schindler et al. 1999). Several subgroups of galaxies are located closely in projected distance and velocity to the Virgo cluster. The galaxy distribution shows mainly a north-south and an east-west elongation. The ICM distribution observed with ROSAT in X-rays (Böhringer et al. 1994) shows a symmetric component around M87 and an asymmetric, low surface brightness emission elongated in north-south direction. The main part of this asymmetric component comes from the galaxy group around the elliptical galaxy M49 located in the south of M87. A small X-ray halo is also associated with M86, a big elliptical galaxy located to the west close to M87.

These asymmetries imply a high dynamical activity. At the same time the Virgo cluster hosts a central cooling flow (White & Sarazin 1988). Since it is thought that a major cluster merger disrupts a central cooling flow (see White et al. (1993) for the Coma cluster), the existence of a symmetric X-ray halo and a cooling flow around M87 thus implies that the Virgo cluster did not experience a major merger in the recent past. Nevertheless, this might happen in the near future (Tully & Shaya 1984).

From the central cD galaxy M87 a distorted radio jet emanates, surrounded by a radio minihalo (Andernach et al. 1979, Rottman et al. 1996, Owen et al. 2000). Its linear extent is about 80 kpc. This minihalo is directly related to the radio jet of M87 and can thus not be qualified as a radio halo as defined above.

We have attempted to detect diffuse radio emission on a Mpc scale in the Virgo cluster at 1.4 GHz with the Effelsberg 100-m telescope. When conducting a search for a presumably weak radio halo from the Virgo cluster, the presence of the quite bright radio source Virgo A (3C274, M87) must be taken into account. At 1.4 GHz the peak flux density is about 150 Jy when measured with the Effelsberg telescope. Such a strong signal produces antenna sidelobes within the area of the cluster what must be adequately taken into account. Another complication arises from the North Polar Spur (NPS), an intense Galactic radio shell, which is likely the old remnant from a nearby supernova explosion. Its minimum distance was previously estimated to be about 100 pc. Its diameter is about  $116^\circ \pm 4^\circ$  (Berkhuijsen et al. 1971). The NPS is seen in projection towards the south-eastern area of the Virgo cluster. Virgo A is close to the outer periphery of the NPS as shown in Fig. 1, where a section of the 1.42 GHz northern-sky Stockert survey (Reich & Reich 1986) is dis-

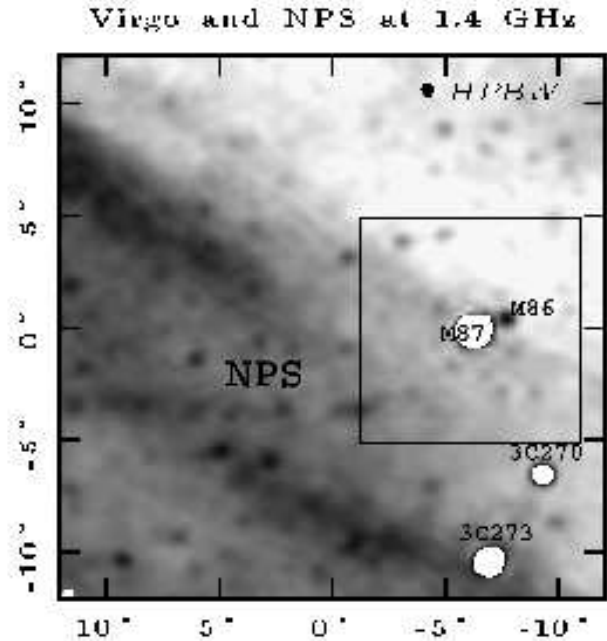


**Fig. 1.** Section of the 1.4 GHz Stockert continuum survey showing a part of the North Polar Spur close to the Virgo cluster with Virgo A or M87 at its center. The greyscale range is between 3.3 K (white) and 3.7 K (black). Intensities above 3.7 K are clipped (shown white). The map is in the equatorial coordinate system and centered at  $12^h57^m18.^s4, 12^\circ24'24''$  (J2000) or  $6^\circ$  to the east of Virgo A. The  $10^\circ \times 10^\circ$  field observed with the Effelsberg telescope is indicated.

played to illustrate the unfavourable situation. However, this absolutely calibrated Stockert survey data may be helpful in a separation of the different contributions.

The observations, data reduction, and the results are described in Sect. 2 followed by the discussion in Sect. 3 and the our conclusions (Sect. 4).

## 2. Observations, data reduction and results

We used the Effelsberg 100-m telescope at 1.4 GHz to map a  $10^\circ \times 10^\circ$  field centered on Virgo A in the equatorial coordinate system. The observations were started in January 2001 and completed in February 2002. Only data from night-time observations were used to avoid any influence by solar sidelobe emission. The field was mapped in orthogonal directions in the equatorial coordinate system by moving the telescope with a speed of  $4^\circ/\text{min}$ . The subscan separation was  $4'$ , which provides full sampling for a beam width (HPBW) of  $9.4'$ . The large size of the field required to split the observations into several sub-fields. In total about two full coverages and in addition some incomplete sections were obtained in both scanning directions. The integration time per pixel was between 4 and 5 sec.

<sup>1</sup> We use a Hubble constant of  $H_0 = 70 \text{ km s}^{-1} \text{ Mpc}^{-1}$ .

Effelsberg continuum and polarization observations with the L-band prime-focus receiver, their reduction and calibration were already described by Uyaniker et al. (1998). In brief, the receiver has two channels for the amplification of the left and right circularly polarized components and is tunable within a frequency range from 1.29 GHz to 1.72 GHz. Cooled HEMT amplifiers reduce the system noise to about 30 K. The drift stability of the system is extremely high that it is operated in total-power mode without any switching. Weather conditions have in practice no influence on the quality of the data. Only in extreme cases of snow and rain fall the noise increases and the baselines are affected. Observations are interrupted in these rare cases. However, impulsive or low level broadband interference was sometimes noted, which needs careful editing. For the observations presented here two IF-polarimeters were used in parallel with center frequencies at 1.395 GHz and 1.408 GHz. The bandwidth of each polarimeter was 14 MHz. The cross-talk between the left and right circular components was found to differ for both subbands and each of them needs to be separately corrected, following in principle the method described by Uyaniker et al. (1998), where the cross-talk of the total-power channels into the polarization channels was canceled. The amount of cross-talk is a few percent of the total intensity signal and is a tribute to the wide frequency range where the receiver can be used.

The calibration of the data relies on the nearby strong radio source 3C286 as the primary calibrator, assuming 14.4 Jy and a percentage polarization of 9.3% at  $33^\circ$  polarization angle. Daily calibration parameters were calculated from the average of all observed calibration sources during a night. The conversion factor from the Jy/beam-scale into main beam brightness temperature was determined by Uyaniker et al. (1998) to  $2.12 \pm 0.02$  K/(mJy/beam). We did not make a spectral correction for the frequency difference of both subbands used.

The raw data were acquired at a rate of 16 msec in  $2 \times 4$  channels. Continuous calibration was applied, where an additional calibration signal was injected for 50% of time. The calibration signal was also used to correct for any phase drift in the IF-polarimeter. The data were interpolated onto a  $4'$  grid along the scanning direction, the same as for the scan separation. Linear baselines were subtracted, which were calculated from a few datapoints at both ends of each scan. This is a standard procedure for single-dish observations, however, only a first step in our case because of the significant influence of the NPS in about half of the map. In addition a systematic negative curvature remains, which reflects the non-linear ground radiation picked up by the telescope's far-sidelobes. This effect may mask or at least reduce any existing symmetric halo centered on Virgo A we aim to detect. For Stokes U and Q linear baseline settings to zero at the edges of the observed map are a compromise as well, since polarized Galactic emission exists everywhere, but requires absolute measurements to get its large-scale level. As an alterna-

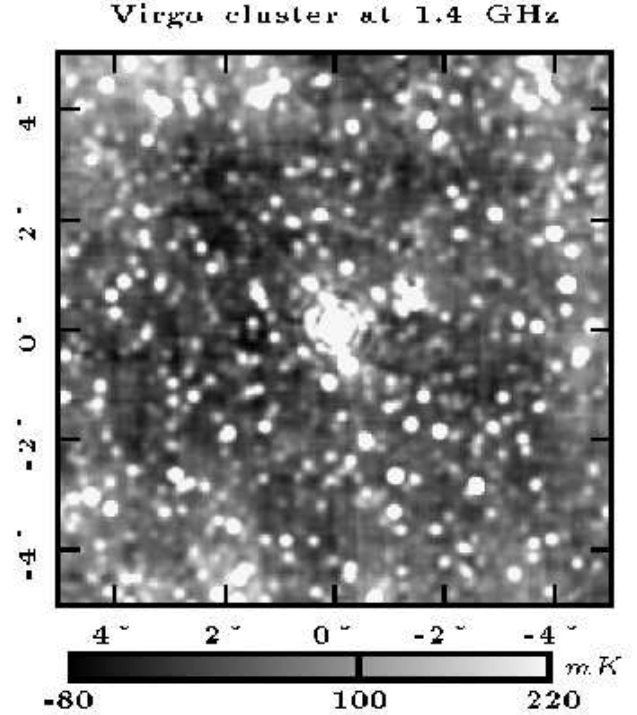


**Fig. 2.** Effelsberg total intensity map of the Virgo cluster centered on Virgo A (M87) at  $12^{\text{h}}30^{\text{m}}49.^{\text{s}}4, +12^\circ23'28.0''$ (J2000). The resolution is  $9'.4$ .

tive, which is mostly used in synthesis telescope observations, the average of a map in U or Q is defined as the zero level.

The observed scans were arranged into maps, edited by standard procedures for spiky interference and baseline distortions of individual scans using an unsharp masking procedure (Sofue & Reich 1979). Correction for cross-talk of the polarization channels and conversion of the raw data into the main beam brightness scale finalizes the raw data reduction. All total intensity maps as well as all U and Q maps were combined using the PLAIT procedure (Emerson & Gräve 1988), which includes a destriping algorithm by weighting down Fourier components along the individual scanning direction of each map. The maps from both subbands were checked for differences, which might show residual interference effects or in the case of U and Q indicate significant Faraday rotation of the polarized emission. However, the differences in U and Q were within the noise and we averaged the maps from both channels in the same way as the total intensity maps.

From the final maps in U and Q we measured a rms-noise of  $\sim 3$  mK  $T_b$  in flat regions. Measuring the rms-noise from the total intensity map is difficult as the map is clearly limited by confusion, which is about 7 mJy/beam or 15 mK  $T_b$  at 1.4 GHz for the Effelsberg telescope (Uyaniker et al. 1999) at a resolution of  $9'.4$ . The measured noise is in the confusion range.

We show the observed I map in Fig. 2. Some systematic total intensity decrease towards the map center is due

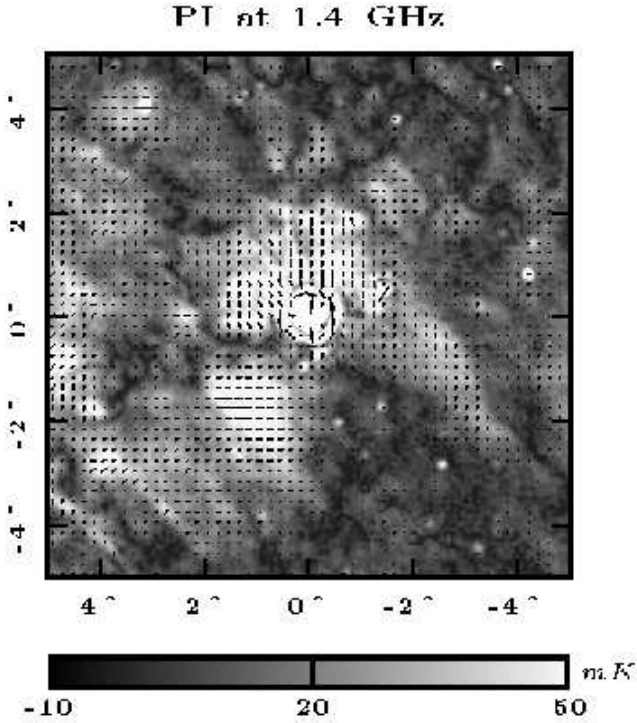


**Fig. 3.** Effelsberg polarized intensity map of the Virgo cluster field centered on Virgo A (M87) at  $12^{\text{h}}30^{\text{m}}49.^{\text{s}}4, +12^{\circ}23'28.0''$  (J2000). The resolution is  $9''.4$ . The lines show the E vectors.

to residual nonlinear ground radiation. The total intensity map shows clear radial sidelobe structures centered on Virgo A due to the four subreflector support legs of the telescope. These limit the dynamic range of the final map to about  $-28\text{dB}$  close to Virgo A after averaging all maps which were observed at different parallactic angles. We tried to further lower these sidelobe responses by taking into account the contribution from the individual maps to the central region. Five maps contribute to the central region which have mean parallactic angles in the range between  $37^{\circ}$  and  $-30^{\circ}$ . Differences of the individual maps compared to the mean map were used to blank regions with strong sidelobes. The fairly uniform ring-like, but weaker diffraction sidelobes remained almost unchanged. In an iterative process the dynamic range could be improved. This method was previously applied to remove the sidelobe response from the subreflector support legs from CAS A, which is stronger than M87, in the Effelsberg 1.4 GHz Galactic plane survey by Reich et al. (1997, their Figs. 1 and 2). The issue how residual sidelobe structures might affect the search for a radio halo is further discussed in Sect. 2.3.

Polarized intensities and polarization angles were calculated from the U and Q maps after they were offset-adjusted so that their mean is zero. The final map of polarized intensity is shown in Fig. 3. The main beam response of U and Q from Virgo A must be considered as residual instrumental polarization and was clipped. In

the ring of first sidelobes some residual instrumental polarization is visible which is on a level of less than 0.1% of the maximum total intensity from Virgo A. Weak radial structures centered on Virgo A have an instrumental origin. Away from Virgo A patchy coherent polarization structures are visible with maximum polarized intensities of about 70 mK (south-east of Virgo A). A number of filamentary structures are running mostly in the direction of the NPS filaments. The NPS is known to be a highly polarized feature in the sky (Spoelstra 1972a, 1972b). The Effelsberg map misses some fraction of this large-scale emission as already mentioned in the context of baseline setting. Since the observed polarized emission is clearly of Galactic origin, we do not consider these data any more in the following analysis.

### 2.1. Source subtraction

In order to increase the sensitivity for diffuse emission, which is clearly limited by confusion of unresolved compact sources, we make use of the NVSS (Condon et al. 1998), a sensitive source survey at 1.4 GHz carried out with the VLA. The survey maps show sources down to about 1 mJy at  $\sim 45''$  angular resolution and are insensitive to all structures exceeding about  $4''.8$ . We combined all NVSS data for the observed  $10^{\circ} \times 10^{\circ}$  field and fitted compact sources down to about 1 mJy with an elliptical Gaussian. Residual sources were tried to be fitted with a more robust, circular Gaussian in a second run. No attempt was made to fit and subtract M87. We constructed a map from the fitted sources which is free of the low-level instrumental artifacts visible in the original NVSS survey maps. This map was convolved to the same angular resolution as the Effelsberg observations. We found the scaling factor for the source map by fitting the slope of an intensity-versus-intensity plot for a number of subsections of the map. The scatter was found to be less than 10%. The convolved and scaled source map was then subtracted from the Effelsberg map. A few residual sources left from the source fitting procedure were removed afterwards. In some cases residuals at the location of strong sources remain. The reasons are a complex source structure not well fitted by a Gaussian, variability, pointing differences between the Effelsberg and the VLA maps or scaling differences in case of strong sources. This procedure reduces the noise-level of the total intensity map to about 4 mK  $T_{\text{b}}$  (3.1 mJy/beam) when convolved to a resolution of  $12''$ . In the following all maps are convolved to a resolution of  $12''$ .

### 2.2. Total intensity baselevel setting

As already mentioned, a systematic negative curvature towards the center of the total intensity map remains, which reflects the non-linear ground radiation picked up by the telescope's far-sidelobes, masking or at least reducing any existing symmetric halo centered on Virgo A we want to detect. We decided to apply three different approaches

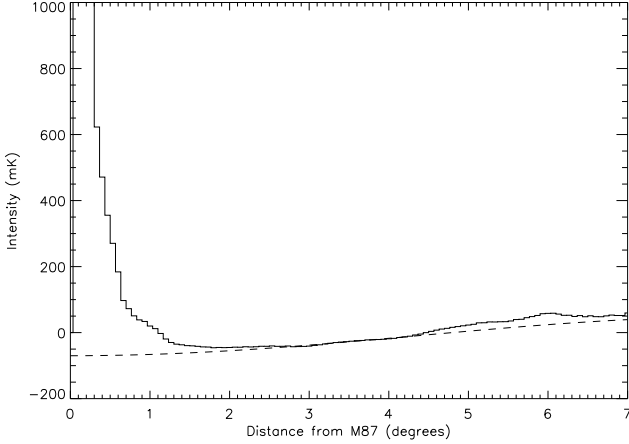


**Fig. 4.** Radial profiles of the Effelsberg 1.4 GHz map where the point sources are subtracted. Solid line: mean radial profile. Dashed line: fitted analytical profile (Eq. 1).

to remove this curvature from the image: (i) subtraction of the mean radial profile of the map, (ii) subtraction of a symmetric analytical profile close to the mean radial profile, and (iii) baselevel correction using an absolutely calibrated map of lower resolution (35').

(i)/(ii) We calculated the mean radial profile of the observed image and then fitted an analytical expression to it

$$S = 60(1 - \cos(20.8 D)) - 70, \quad (1)$$

where  $D$  is the distance from M87 in degrees (Fig. 4) and  $S$  is in mK. These profiles were subtracted from the total power image where the point sources are subtracted, whereas the sidelobes are still included (Figs. 5 and 6). In this way we only investigate the influence of the baselevel subtraction. Since in the analytic expression the central peak is not included, M87 appears entirely in Fig. 6, whereas only its sidelobes remain in Fig. 5. The distributions of the diffuse, extended emission are very similar for both images. The structures that are elongated in the north-east towards south-west direction most likely belong to the NPS. A region of diffuse emission can be seen north-west of M86 with a linear extent of  $\sim 1.5^\circ$ . This feature does not show a north-west elongation typical for the NPS and thus most probably originates in the Virgo cluster.

(iii) We use the section of the absolutely calibrated Stockert 1.4 GHz survey map (Reich & Reich 1986) to correct the source-subtracted Effelsberg map first for absolute baselevels and then for flat baselevels across the  $10^\circ$  field in order to identify extended emission from the Virgo cluster. The Stockert map at  $35'$  was first decomposed into its large scale ( $\geq 2^\circ$ ) emission using the 'background filtering method' by Sofue & Reich (1979). The Effelsberg map was convolved to an angular resolution of  $2^\circ$  and the difference to the large-scale structures from the Effelsberg map was added to the Effelsberg map at its original angular resolution. The general gradient in the map from

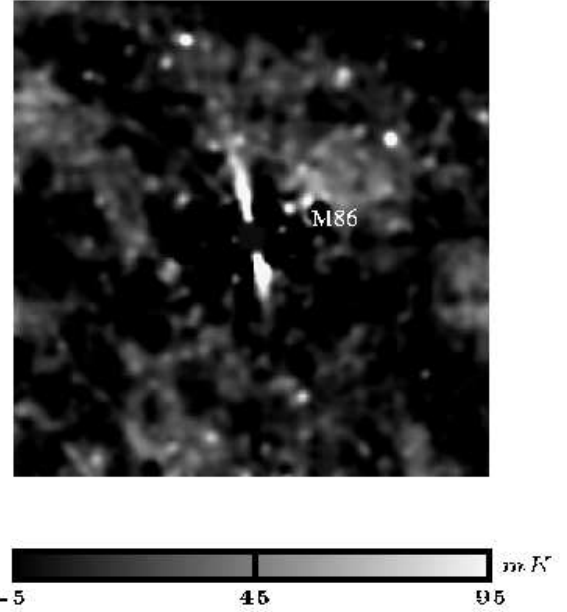


**Fig. 5.** Effelsberg 1.4 GHz total power map (Fig. 2) where the point sources and the mean radial profile are subtracted. The resolution is  $12'$ . The RA and DEC axis are the same as in Fig. 2. The location of M86 is indicated.

north-west to south-east due to the presence of the large-scale NPS emission (see Fig. 2) was further reduced by applying again the 'background filtering method' with a  $2^\circ$  filter beam to remove the large-scale gradient. Finally small offsets were taken from ring integration to set the average zero level at about  $4^\circ$  distance from Virgo A. The result of this procedure is shown in Fig. 7. As in Figs. 5 and 6 emission of the NPS has a characteristic elongation from north-east towards south-west and is visible in the south-eastern quadrant of the image. At this low surface brightness level the residuals of the sidelobes around M87 can be seen mainly to the north and south of M87 (compare with Fig. 5). The bright structures surrounding M86 are most probably also due to sidelobes of M86. However, the large, low surface brightness emission at larger distances from M86 is the same as the one observed in Figs. 5 and 6. It is further discussed in Sect. 2.4.

### 2.3. Sidelobe response

We are interested in weak diffuse emission structures in the surrounding area of Virgo A and need to know its sidelobe contribution to a very low level. Deep observations of the antenna characteristics at 1.4 GHz are difficult using strong and compact celestial sources like Cas A, Cygnus A or Taurus A, as they have Galactic emission structures in their surroundings as well as extragalactic compact sources exceeding the telescope's sidelobe response in intensity and are difficult to separate. Since no actual antenna pattern is available at 1.4 GHz no full cleaning like

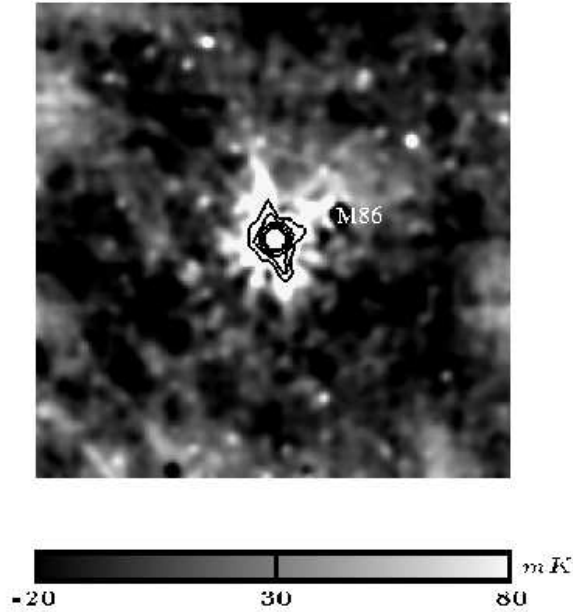


**Fig. 6.** Effelsberg 1.4 GHz total power map (Fig. 2) where the point sources and the analytically fitted profile are subtracted. The resolution is  $12'$ . The RA and DEC axis are the same as in Fig. 2. The contours show the radio emission of M87. The location of M86 is indicated.

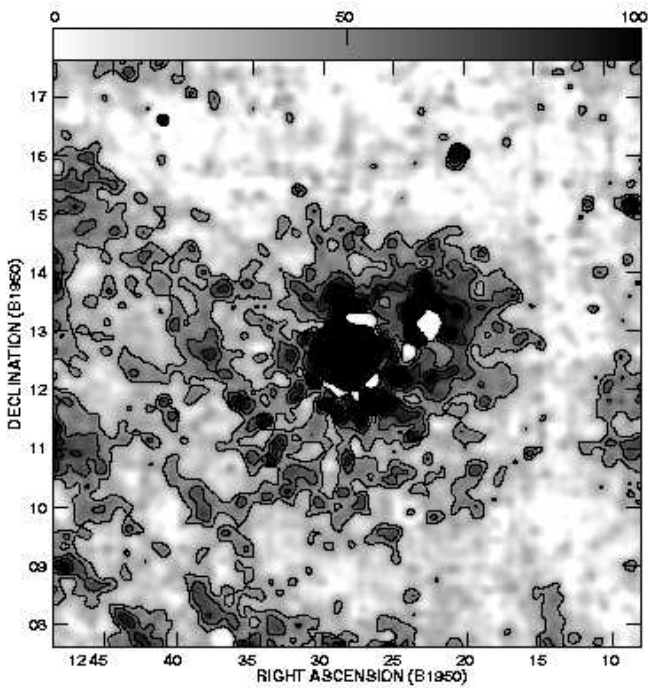


**Fig. 7.** Effelsberg 1.4 GHz total power map (Fig. 2) where the point sources are subtracted, the sidelobes are removed, and the large-scale structure is added. The resolution is  $12'$ . The greyscale runs from 0 to 100 mK. The contours are (1, 1.5, 2, 2.5, 3, 4, 5, 6, 7, 8, 9, 10) 40 mK. At  $12'$  1 mK corresponds to 0.77 mJy/beam.

that applied by Rottmann et al. (1996) at 10 GHz was possible. Therefore we were limited to remove only the strongest sidelobe structures from the subreflector support legs as described above, but we will show that the residual diffraction sidelobes from M87 are weaker than the halo emission we are looking for.

Kalberla et al. (1980) have made antenna pattern measurements of the Effelsberg 100-m telescope at 1.4 GHz using Cas A and separated the antenna sidelobes from sky emission by comparing measurements at different parallactic angles. The sun was used in addition to measure a small area with the telescope's far-sidelobes at  $60^\circ$  to  $65^\circ$  distance. Kalberla et al. (1980) measure within  $1^\circ$  to  $4^\circ$  distance from the main beam patchy sidelobe structures within  $-40$ dB and  $-45$ dB (their Fig. 2). This level excludes the clearly enhanced cross-like structures from the slit diffraction pattern of the four feed support legs.

Meanwhile more detailed information on the telescope's sidelobes structures became available in the course of holographic measurements using geostationary satellites. Their beacons are so strong that any sky emission does not confuse with the sidelobe structures. These measurements, however, are made at high frequencies and need appropriate scaling to be comparable with the 1.4 GHz sidelobe structure. We used for comparison the antenna pattern measured by Reich & Fürst (2000) using the beacon onboard EUTELSAT at 11.7 GHz. The edge taper of the 11.7 GHz feed was lower than that of the L-band feed to have sufficient sensitivity for the adjustment of the outer telescope panels based on the holographic result. Therefore the antenna pattern at 11.7 GHz when scaled to 1.4 GHz is expected to show slightly higher sidelobe levels than present at 1.4 GHz. In addition the telescope surface deviations from the ideal parabolic shape enhance the high frequency sidelobe levels more than those of the L-band. A comparison of the scaled and ring-averaged 11.8 GHz pattern with ring-integrated emission from the map shown in Fig. 7 is displayed in Fig. 8. We show the emission in the M86 quadrant (position angles  $0^\circ$  to  $90^\circ$ ). From the 11.8 GHz pattern the contribution of the four subreflector support legs was excluded from the ring integration. Clearly the antenna sidelobe levels are below  $-40$ dB for radii larger than about  $60'$  and drop to below  $-55$ dB beyond  $180'$ . The emission measured in the M86 area is clearly higher than any instrumental effect and also higher than the emission measured in the other quadrant, which includes some low-level filamentary fine structures which are likely from the NPS according to their general orientation. The emission profiles depend on the adopted zero levels, which we have defined at a radial distance of  $40'$  from Virgo A. The uncertainty is estimated to about 5 mK, which has an effect of less than 1dB at the  $-40$ dB level and about 6dB at the  $-50$ dB level for example.

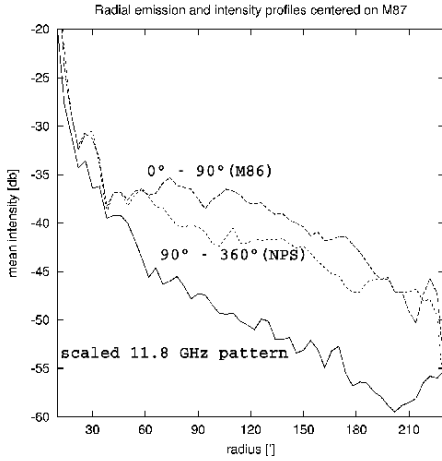


**Fig. 8.** Radial intensity profiles measured at 11.8 GHz using the EUTELSAT satellite and scaled to 1.4 GHz in comparison with mean radial intensities measured in the sectors  $0^\circ - 90^\circ$  and  $90^\circ - 360^\circ$  (counterclockwise from north) from the map shown in Fig. 7.

#### 2.4. The M86 radio halo

Based on Figs. 5, 6, 7, and 8 the radio halo around M86 is a robust feature of low surface brightness ( $\sim 50$  mK or  $\sim 38$  mJy/(12' beam) at a distance of about  $1^\circ$  from M86). Its radial extent is  $\sim 2^\circ$  to the west. It is not possible to determine its extent to the east because of the emission of M87 and its sidelobe residuals. In Figs. 5 and 6 the M86 radio halo appears to be asymmetric, which is mainly due to the way how the radially symmetric emission was subtracted. Thus it is unclear whether the M86 radio halo is symmetric or not.

For an estimate of its total 1.4 GHz flux we adopted two strategies: (i) We assume an asymmetric radio halo and integrate the emission in incomplete rings centered on M86 up to a distance of  $2^\circ$ . The area close to M87 (right ascension offset  $< -36'$ ) was excluded. In this way we derive a lower limit for the flux density of  $4.7 \pm 1.4$  Jy. (ii) We assume a symmetric Gaussian distribution with a HPW of  $2^\circ$  and a peak intensity of 80 mK at 12' resolution. In this case the halo flux density is about  $6.1 \pm 1.2$  Jy for an estimated error of 20%, which we take as an upper limit. Combining both results we quote  $5 \pm 1.5$  Jy for the halos flux density.

### 3. Discussion

The analysis of our 1.4 GHz Effelsberg data has shown that the Virgo cluster does not host a bright, large-scale radio halo. However, we cannot exclude the existence of a weak radio halo centered on M87 of a diameter smaller than  $4^\circ$  ( $\sim 1.2$  Mpc) with a surface brightness smaller than one third of the radio halo in the Coma cluster. The detected M86 radio halo is smaller in size and not located in the cluster center as is the case for the Coma cluster radio halo (see e.g. Deiss et al. 1997). Its radial extent to

the west is  $\sim 2^\circ$ . We cannot determine whether the M86 radio halo is symmetric or not because of its proximity to M87. It is not excluded that the M86 halo comprises M87 and that the center is located between M86 and M87. This would resemble the large-scale structure of the X-ray structure (Finoguenov et al. 2004). As already mentioned in Sect. 1 the Virgo cluster is classified as a cooling flow cluster. Since radio halos avoid this kind of galaxy clusters, this is an expected result.

However, we detect a radio halo around the elliptical galaxy M86. Despite the complex data reduction (sidelobes, ground emission, point sources) this result is robust (see Sect. 2) and entirely unexpected. The radio halo appears to be more extended to the north-west (Figs. 5, 6, 7), but the data do not allow to derive a firm conclusion. Why should M86 harbour a radio halo? If we assume that a radio halo witnesses a past interaction, one possibility is that the ICM of M86 has interacted with the ICM of M87, i.e. of the Virgo cluster, in the past. In this case M86 is falling into the Virgo cluster from behind (its radial velocity is  $-1350$  km s $^{-1}$  with respect to the cluster mean velocity).

Finoguenov et al. (2004) observed M86 in X-rays with the XMM-Newton telescope. They found a shock in the south-west of the galaxy center. Since Neilsen & Tsvetanov (2000), using the method of surface brightness fluctuations, place M86 at  $2.4 \pm 1.4$  Mpc behind the cluster, Finoguenov et al. (2004) concluded that M86 is not interacting with the Virgo ICM, but with a filament detected in the ROSAT observations (Böhringer et al. 1994). Moreover, Finoguenov et al. (2004) claimed that the asymmetric, high surface brightness X-ray distribution of M86 is due to close, high velocity galaxy–galaxy interactions. They also noted that the X-ray halo around M86 is relatively symmetric, but there is an offset between the center of the large-scale distribution and the location of M86, which is displaced to the south-east (their Fig. 12). This offset is consistent with the M86 halo asymmetry we observe in our radio data. The fact that M87 does not show a bright large-scale halo might indeed indicate that M86 has not yet passed M87, or that it has passed M87 very recently so that the halo is not built yet.

On the other hand, the distribution of dwarf galaxies (Schindler et al. 1999) around M87 is asymmetric with its maximum located between M87 and M86. A possible explanation is that M86 has already passed M87 and that M87 is moving (see Vollmer et al. 2001) or that the dwarf galaxies follow the perturbed gravitational potential with a certain delay.

We are thus left with two possible scenarios:

- (i) M86 is entering the cluster from behind and is located at a distance  $D > 2$  Mpc.
- (ii) M86 has just passed M87 and a radio halo has not yet been built around M87.

It is not clear how galaxy–galaxy interactions that act on scales between 10 kpc and 50 kpc at most can give rise to a radio halo of 600 kpc. In contrast, a large-scale shock in the ICM due to an ICM–ICM interaction between M86

and M87 can do it. Thus, the radio halo of M86 is most probably due to an interaction between the ICM of M86 and a large-scale gas structure with a density much smaller than  $10^{-4} \text{ cm}^{-3}$ . The M86 radio halo has a linear extent of  $\sim 0.6 \text{ Mpc}$ . After an interaction, the reverse shock wave that travels with a sound speed of  $\sim 500 \text{ km s}^{-1}$  needs  $\sim 1 \text{ Gyr}$  to cross the halo. This is about the timescale to build a radio halo. The radio halo is thus reminiscent of a past interaction of the M86 ICM with a low density gas, whereas the X-ray morphology is due to a recent interaction of the M86 ICM with a relatively high density gas.

If M86 was about 2 Mpc away from the cluster center, it would have been about 3 Mpc away at the time of the beginning of the interaction (assuming a velocity of  $1300 \text{ km s}^{-1}$ ). At a distance of 2 Mpc the Virgo ICM density is far below  $10^{-4} \text{ cm}^{-3}$  (Schindler et al. 1999). Why should there be a gas filament of a density of several  $10^{-4} \text{ cm}^{-3}$ ? We do not see how there can be such a large density contrast of the gas that interacts with the M86 ICM between 3 Mpc (beginning of the large-scale interaction) and 2 Mpc (small-scale interaction). This density gradient is naturally found further inside the cluster. Therefore, we prefer scenario (ii), where the interaction began at a distance of  $\sim 1 \text{ Mpc}$  to 2 Mpc from the cluster center. This interaction decelerated the outer ICM of M86 whereas M86 itself continued its way into the Virgo cluster where it now meets Virgo ICM gas densities of several  $10^{-4} \text{ cm}^{-3}$ . It might be near M87, making it move or trailing the dwarf galaxies behind it. This scenario explains naturally the high ICM density needed to produce the observed shock and the high velocity galaxy–galaxy encounters needed to explain the high surface brightness X-ray morphology of M86, since high-speed encounters are more probable in the cluster core where the galaxy density is higher.

#### 4. Conclusions

We present Effelsberg 1.4 GHz observations of the central  $10^\circ \times 10^\circ$  of the Virgo cluster, in order to investigate if the cluster hosts a diffuse radio halo. Three major obstacles have to be overcome to detect a large-scale, low surface brightness structure: (i) the North Polar Spur (NPS) extends into the Virgo cluster region, (ii) the high flux density of the central cD galaxy M87 leads to strong sidelobes, and (iii) the ground radiation due to the large scans. The NVSS survey is used to subtract the point sources from our total intensity map. In this way we decrease the rms noise level from 7 mJy/beam at a resolution of  $9.4''$  to 3 mJy/beam at a resolution of  $12''$ . In the total intensity and polarized intensity map the NPS appears as elongated structures running along the north-east towards south-west direction in the south-eastern part of the maps. Parts of the NPS extend up to the location of M87. We corrected for the non-linear ground radiation in three ways: (i) we subtracted the observed mean radial profile, (ii) we subtracted an analytical profile, and (iii) we corrected for the

large-scale structure with the help of absolutely calibrated 1.4 GHz observations of lower resolution. The remaining sidelobe confusion is analyzed using a holographic, deep antenna pattern at 11.7 GHz using the EUTELSAT satellite.

It is concluded that

1. we do not detect a bright, large-scale radio halo, as it is observed in the Coma cluster.
2. We detect a radio halo around the elliptical galaxy M86 with an estimated radial extent of  $\sim 2^\circ$  and an estimated total flux density of  $5 \pm 1.5 \text{ Jy}$ .
3. The detection of the M86 radio halo is robust.
4. The radio halo is a witness of a past interaction of the M86 ICM with low density gas at the outskirts of the Virgo cluster.
5. This leads to a scenario where the ICM of M86 had an interaction  $\sim 1 \text{ Gyr}$  ago with a low density gas, whereas M86 itself undergoes an interaction with a relatively high density gas today (Finoguenov et al. 2004).

*Acknowledgements.* We would like to thank A. Finoguenov for useful discussions.

#### References

- Andernach H., Baker J. R., von Kap-herr A., & Wielebinski R. 1979, *A&A*, 74, 93
- Berkhuijsen E. M., Haslam C. G. T., & Salter C. J. 1971, *A&A* 14, 252
- Böhringer H., & Schücker P. 2002, in: *Merging Processes in Galaxy Clusters*, Ed. L. Feretti, I.M. Gioia, & G. Giovannini, *Astrophysics and Space Science Library*, Vol. 272 (Dordrecht: Kluwer) p. 133
- Böhringer H., Briel U. G., Schwarz R. A. et al. 1994, *Nature*, 368, 828
- Brouw W. N., & Spoelstra, T. A. Th. 1976, *A&AS*, 26, 129
- Condon J. J., Cotton W. D., Greisen E., et al. 1998, *AJ*, 115, 1693
- Deiss B. M., Reich W., Lesch H., & Wielebinski R. 1997, *A&A*, 321, 55
- Ebeling H., Voges W., Böhringer H., et al. 1996, *MNRAS*, 281, 799
- Emerson D. T., & Gräve R. 1988, *A&A* 190, 353
- Finoguenov A., Pietsch W., Aschenbach B., & Miniati F. 2004, *A&A*, 415, 415
- Giovannini G., & Feretti L. 2002a, in: *Merging Processes in Galaxy Clusters*, Ed. L. Feretti, I. M. Gioia, & G. Giovannini, *Astrophysics and Space Science Library*, Vol. 272 (Dordrecht: Kluwer) p. 197
- Giovannini G., & Feretti L. 2002b, in: *Highlights of Astronomy*, Vol. 12, as presented at the XXIVth General Assembly of the IAU - 2000 [Manchester, UK, 7 - 18 August 2000]. Ed. H. Rickman (San Francisco: Astronomical Society of the Pacific) p. 513
- Kalberla P. M. W., Mebold U., & Reich, W. 1980, *A&A*, 82, 275
- Neilon E. H., & Tsvetanov, Z. I. 2000, *ApJ*, 536, 255
- Owen F. N., Eilek J. A., & Kassim N. E. 2000, *ApJ*, 543, 611
- Reich P., & Reich W. 1986, *A&AS*, 63, 205
- Reich P., Reich W. & Fürst E. 1997, *A&AS*, 126, 413



- Reich W., & Fürst E. 2000, Kleinheubacher Berichte, 43, 175
- Röttgering H. J. A., Wieringa M. H., Hunstead R. W., & Ekers R. D. 1997, MNRAS, 290, 577
- Rottmann H., Mack K.-H., Klein U., & Wielebinski R. 1996, A&A, 309, L19
- Schindler S., Bingelli B., & Böhringer H. 1999, A&A, 343, 420
- Sofue Y., & Reich W. 1979, A&AS, 38, 251
- Spoelstra T. A. Th. 1972a, A&AS, 5, 205
- Spoelstra T. A. Th. 1972b, A&A, 21, 61
- Tully R. B. & Shaya E. J. 1984, ApJ, 281, 31
- Uyaniker B., Fürst E., Reich W., Reich P., & Wielebinski R. 1998, A&AS, 132, 401
- Uyaniker B., Fürst E., Reich W., Reich P., & Wielebinski R. 1999, A&AS, 138, 31
- White S. D. M., Briel U. G., & Henry J. P. 1993, MNRAS, 261, L8
- White R. E. & Sarazin C. L. 1988, ApJ, 335, 688